RSC Advances

PAPER

View Article Online
View Journal | View Issue

Cite this: *RSC Adv.*, 2020, **10**, 2989

Microstructure and electrochemical performance of 3D hierarchical porous graphene/polyaniline composites

Zhaoxia Hou,* Lingxi Kong, Shengnan Zou, Lanwei Zhao and Lirong Yang

Received 10th September 2019
Accepted 20th December 2019

DOI: 10.1039/c9ra07248a

rsc.li/rsc-advances

Porous graphene materials show outstanding performance in energy storage field due to their unique microstructure and properties. To construct 3D hierarchical porous graphene and combine with conductive polyaniline is an effective way to realize high energy density and good cycling stability. The interlamellar macroporous structure of 3D graphene was constructed by polystyrene (PS) microspheres and nickel foam as double templates. The mesoporous structure was etched in 3D macroporous graphene sheets by potassium hydroxide (KOH) chemical activation. And 3D hierarchical porous graphene (3D-hpGr) composited with polyaniline (PANI) by *in situ* chemical oxidative polymerization to obtain 3D-hpGr/PANI composites. The effect of the introduction of 3D-hpGr on microstructure, morphology and electrochemical performance of the composites was investigated. PANI nanowire arrays successfully decorate the surface of the 3D-hpGr sheets when the amount of 3D-hpGr reaches 40% (wt%). The specific capacitance of 3D-hpGr/PANI40 reaches 573 F g^{-1} at 0.5 A g^{-1}, much higher than that of pure PANI (419 F g^{-1}). The retention ratio of 3D-hpGr/PANI40 retains 84% of its initial specific capacitance after 1000 cycles at 1.0 A g^{-1}, and the cycling stability of all composites is higher than that of pure PANI (69%). The potential drop of 3D-hpGr/PANI composites decreases from 0.339 V to 0.139 V, and the energy density increases consequently. The energy density of 3D-hpGr/PANI40 reaches 31.2 W h kg^{-1} at the power density of 0.709 kW kg^{-1}.

1 Introduction

Supercapacitors are considered as promising candidates in digital products, power devices and hybrid electric vehicles *etc.*, owing to their outstanding features of rapid charge/discharge, long service life and high power density.[1] The theoretical specific capacitance of graphene can be as high as 550 F g^{-1}.[2] However, irreversible agglomeration occurs between graphene sheets due to the π–π bond stacking and van der Waals forces, which makes the capacitor performance unsatisfactory.[3] In order to successfully exploit the excellent properties of graphene for electrochemical applications, the re-stacking of graphene sheets needs to be minimized.[4] Compared with other porous carbon materials, graphene-based porous materials have high mechanical strength, a large specific surface area, good chemical and thermal stability, and high electrical conductivity, and are easy to be combined with other organic and inorganic materials.[5] Porous graphene materials show outstanding performance in the energy storage field due to their unique microstructure and properties.[6–8] The pore size, pore shape, and pore volume of the porous graphene material are critical to the performance. Therefore, it is of great research significance to build a unique porous structure of graphene in order to improve its application value in various high performance devices.

Graphene-based porous materials can be divided into single-layer porous graphene (with in-plane pores),[9] 2D-layered porous graphene (interlayer pores)[10] and 3D porous graphene networks (including in-plane pores and 3D cross-linking).[11] Although the size of the interlayer pores of the 2D-layer porous graphene can be precisely controlled by adjusting the structure of the intercalating molecule and the type of intercalating agent, the adjustable range is relatively limited, ranging from sub-nanometer to several nanometers, this scale is not sufficient for electrochemical applications.[6] Therefore, 2D graphene nanosheets are constructed into a 3D porous structure, on the one hand, the intrinsic structure and characteristics of graphene can be partially retained, on the other hand, the large specific surface area can be realized, which is favorable for electrochemical storage. In addition, the formation of the in-plane pores and the 3D porous network may provide effective conditions for transport of electrolyte ions and interaction between electrolyte ions and electrode materials.[12]

Typical conducting polymers—polyaniline (PANI) and its composites have been studied recently due to its easy synthesis, low cost, easy doping and high pseudocapacitance.[13–17]

Liaoning Province Key Laboratory of Micro-Nano Materials Reseaerch and Development, School of Mechanical Engineering, Shenyang University, Shenyang 110044, China. E-mail: luckyxia2007@126.com

However, the cycling stability of PANI is usually poor and its rate capability is low, which was mainly owing to the mechanical deterioration and the slow charge transfer.[18] The combination of 3D hierarchical graphene with controllable morphology conductive PANI can prevent the re-stacking of graphene, and graphene itself can inhibit the mechanical deterioration of PANI during charge and discharge. In addition, the 3D porous structure can provide space for the expansion and contraction of PANI and accelerate the transmission rate of ions in the active electrodes.

In this work, the graphene oxide (GO) prepared by the modified Hummers' method was used as the precursor, the interlamellar macroporous structure of 3D graphene was constructed by polystyrene (PS) microspheres and nickel foam as double templates. Then, the mesoporous structure was etched in 3D graphene sheets by KOH chemical activation, and finally a 3D hierarchical porous graphene (3D-hpGr) was formed. And then graphene with 3D hierarchical porous structure composited with PANI by the *in situ* polymerization. The synthesis process was shown in Scheme 1. The microstructure, morphology and electrochemical performance of 3D-hpGr/PANI composites were characterized and investigated. The 3D-hpGr/PANI composites showed a high specific capacitance, good cycling stability and high-energy density.

2 Materials and methods

2.1 Materials

All reagents are analytically pure and were used directly without any further treatment. Graphite powder (25 μm) came from Nanjing XFNANO Materials Tech Co., Ltd. Aniline (An), ammonium persulfate (APS) and sodium hydrosulfite were obtained from Tianjin Damao Chemical Agent Company. Potassium hydroxide (KOH), polyvinylpyrrolidone K30 (PVP), and azobisisobutyronitrile (AIBN) were purchased from Tianjin Bodi Chemical Engineering Corporation. Styrene (ST) was acquired from Shandong West Asia Chemical Industry Co., Ltd. Nickel foam was obtained from Shenzhen Green Tech.

2.2 Preparation of PS microspheres

PS microspheres were synthesized by the dispersion polymerization method. Deionized water 20 mL and isopropanol 140 g were mixed, the mixture was then added PVP 3 g, kept stirring at 70 °C, then added AIBN 1.0 g and ST 50 g. The solution above was magnetically stirred at 70 °C for 24 h under a nitrogen atmosphere. The PS emulsion was centrifuged, washed repeatedly with ethanol and deionized water, and then dispersed in deionized water to obtain a PS suspension, finally dried in an oven at 50 °C for further amination.

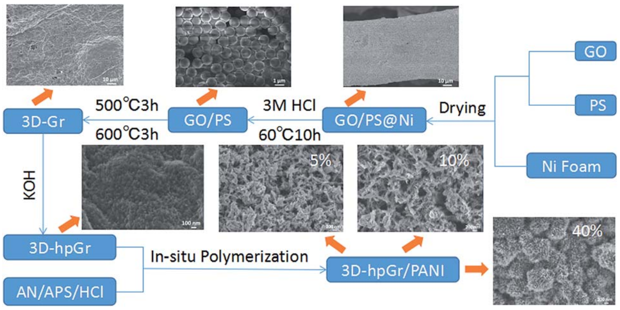

Scheme 1 Schematic representation of synthesis process of 3D-hpGr/PANI.

PS microspheres were nitrated and then aminated to make them charge positively. The nitration process is as follows: 100 g 10% PS emulsion with deionized water as dispersant was magnetically stirred at 50 °C, and then mixed with 50 mL nitric acid and sulfuric acid with the volume ratio of 2 : 3. The reaction kept going at room temperature for 2 h, and then the emulsion was filtered, and washed repeatedly with deionized water until the pH value was neutral. The nitrated polystyrene (PNS) was dried in an oven at 50 °C for 24 h, the pale yellow PNS powders were stored in a refrigerator for use. The amination process was as follows: the above PNS powders were put into a flask, then 60 mL of 2 M NaOH solution was added, and magnetic stirring was carried out at 75 °C, then the reducing agent $Na_2S_2O_4$ was added. The reaction was kept going at 75 °C for 4 h, and the emulsion was filtered, and washed repeatedly with deionized water until the pH value was neutral. Finally, the aminated polystyrene (PAS) were dried in an oven at 50 °C for 24 h, the yellow PAS powders were stored in the refrigerator for use.

2.3 Preparation of 3D macroporous graphene

GO was prepared by a modified Hummers' method according to the ref. 19. The 1 mg mL^{-1} GO dispersion mixed with the 10 wt% PAS emulsion at a mass ratio of 2 : 1. GO and PAS dispersion was kept stirring for half an hour and dispersed by ultrasound for 3 h. Since the PAS positively charged and GO negatively charged attract each other, GO can fully wrapped on the surface of PS microspheres. The nickel foam was washed by 0.1 M HCl and immersed in a GO/PS dispersion for 30 min and dried at 50 °C for 6 h, repeated the operation for three times to ensure that the GO/PS adhered evenly on the surface of the nickel foam, and the sample was marked as GO/PS@Ni. Finally, GO/PS@Ni was immersed in 3 M HCl and heat-treated at 60 °C for 10 h to remove the nickel foam. GO/PS removal Ni was filtered, and washed repeatedly with deionized water until the pH value was neutral, and then heat treated in a tube furnace at 500 °C for 3 h and 600 °C for 3 h to remove the PS templates. Thus, 3D macroporous graphene (3D-Gr) was obtained.

2.4 Preparation of 3D-hpGr

7 M KOH solution was stirred with 3D-Gr for 30 min, the mass ratio of KOH to 3D-Gr was 7 : 1. The dispersion was allowed to stand for 24 h at room temperature, then freeze-dried for 48 h, and the dried sample was heat treated in a tube furnace at 500 °C for 5 h under a nitrogen atmosphere. The product was repeatedly rinsed with 36% acetic acid and deionized water until the pH value was neutral, and then 3D-hpGr was obtained.

2.5 Preparation of 3D-hpGr/PANI composites

3D-hpGr/PANI composites were synthesized by the *in situ* chemical oxidative polymerization method with An as a monomer in the presence of 3D-hpGr. The procedures were as followed: 3D-hpGr was ultrasonically dispersed in 1 M HCl for 0.5 h, and 30 mM An was added into 3D-hpGr suspension, and performed another 0.5 h sonication, and then decreased to 0 °C. APS was dropped in, and kept stirring at 0 °C for 24 h, the molar ratio of An to APS is 10 : 1. The composites were repeatedly filtered and washed with deionized water and ethanol, until the filtrate became colorless. Composites were marked as 3D-hpGr/PANI5, 3D-hpGr/PANI10, and 3D-hpGr/PANI40 according to the weight percent of 3D-hpGr, respectively; such as 3D-hpGr/PANI5 represents that 3D-hpGr accounts for 5% (wt%). In order to comparison, pure PANI was synthesized *via* the same procedures described above but without 3D-hpGr.

2.6 Materials characterization

X-ray diffraction (XRD, PANalytical) was analyzed with Cu Kα radiation ($\lambda = 0.15418$ nm) from 5° to 60°. Fourier transform infrared spectrometer (FT-IR, Bruker EQUNOX 55) was recorded at room temperature from 400 cm^{-1} to 4000 cm^{-1} at a resolution of 2 cm^{-1} with KBr powder pellet. The microstructure was observed by the Field Emission Scanning Electron Microscope (FE-SEM, Hitachi S4800) and Transmission Electron Microscope (TEM, Japanese electronic JME-2100).

The electrodes were manufactured by active materials with 10% binder (polytetrafluoroethylene). The two-electrode system was assembled with the carbon fibre paper as a current collector, the cellulose paper as a separator, and 1 M H_2SO_4 aqueous as the electrolyte. Electrochemical impedance spectroscopy (EIS), cyclic voltammetry (CV) and galvanostatic charge–discharge (CD) measurements were carried out in the two-electrode system. CV and EIS were tested on a PARSTART 2237 electrochemical workstation. CD was carried out by the supercapacitor test system CT2001A of Wuhan Blue Electric. CV and CD measurements were performed within the potential range of 0–0.8 V. CV curves were tested at scan rates of 5, 10, 25, 50, and 100 mV s^{-1}. CD curves were set in the range from 0.01 Hz to 100 kHz at different current densities.

The specific capacitance (C_s) of the material based on CD data is determined according to the eqn (1):

$$C_s = \frac{4I\Delta t}{m\Delta V} \tag{1}$$

where, I is discharge current (A), Δt is the discharging time (s), m is the total mass of active material (g), and ΔV is the voltage drop (V).

The eqn (2) is used to calculate the energy density E of supercapacitor,

$$E = \frac{C_s\Delta V^2}{8} \tag{2}$$

The eqn (3) is used to calculate the power density P of supercapacitor,

$$P = \frac{E}{\Delta t} \tag{3}$$

3 Results and discussion

3.1 Microstructure and morphology

Fig. 1(a) is a SEM image of PS microspheres synthesized by the dispersion polymerization method. It can be seen that microspheres have a smooth surface, good monodispersity, the uniform spherical diameter of about 1.2 μm. SEM image of the GO/PS sample is shown in Fig. 1(b). It can be seen that GO is uniformly coated on the surface of PS microspheres, and wrinkles of GO are clearly visible at the edge of PS microspheres, indicating that GO sheets are very thin. Fig. 1(c) and (d) are SEM images of GO/PS@Ni and GO/PS after nickel removal, respectively. It can be seen from Fig. 1(c) that GO/PS covered uniformly and completely on nickel foam after three times of dip coating. PS/GO retains the skeleton structure of nickel foam after removal of nickel foam (Fig. 1(d)).

The result of EDS (Fig. 1(e)) shows that the element Ni is completely removed. Fig. 1(f) is the SEM of 3D-Gr after removal PS and nickel foam templates, it can be seen obviously that there exist a lot of pores sized at about 1 μm formed by PS. It can be seen from Fig. 1(f) that the PS microspheres have been removed after being treated at 500 °C for 3 h and 600 °C for 3 h. Thus 3D-Gr is formed successfully by using PS and nickel foam double templates, laying the foundation for the subsequent architecture of 3D-hpGr.

SEM images of 3D-hpGr obtained after KOH activation are shown in Fig. 2(a–c) and (d) is before KOH activation. It can be seen that there are significant change after KOH activation. Holes with the size of ~1 μm can be observed on graphene sheets (Fig. 2(a)). After further enlargement, it is found that there exist a large number of dense mesopores on the surface (Fig. 2(b)) and the surrounding (Fig. 2(c)) of the holes, 3D hierarchical pore structure forms after high temperature KOH activation.

The XRD patterns of 3D-hpGr, pure PANI, 3D-hpGr/PANI5, 3D-hpGr/PANI10, and 3D-hpGr/PANI40 are shown in Fig. 3. The apparent diffraction peaks at 25.0° and 43.0° are attributed to the (002) and (100) crystal planes of graphene. In addition, there are no other diffraction peaks in 3D-hpGr, indicating PS microspheres and Ni have been completely removed. Four distinct diffraction peaks around 9.8°, 15.3°, 20.2°, and 24.8° can be seen from composites and pure PANI, corresponding to (001), (011), (020), and (200) crystal planes of PANI (JCPDS53-1891), respectively.

Fig. 4 shows the FT-IR spectra of PS, GO/PS, 3D-hpGr, pure PANI, 3D-hpGr/PANI5, 3D-hpGr/PANI10, and 3D-hpGr/PANI40. It can be seen from the spectrum of PS that there exist six obvious peaks around 3025, 2922, 1493, 1452, 757 and 689 cm^{-1}, 3025 cm^{-1} corresponds to the asymmetric stretching vibration of C–H in –CH_2—, 2922 cm^{-1} corresponds to the stretching vibration of the aromatic C–H,[20,21] 1493 and 1452 cm^{-1} are attributed to bending vibration of C–H in –CH_2–, 757 and 689 cm^{-1} are attributed to the out-plane bending vibration of the aromatic C–H. Theses peaks all disappear from the spectrum of 3D-hpGr, which indicates that PS has been removed. While GO/PS obviously appears both of the characteristics of PS and GO, so it further testified the result of GO coating on PS from SEM analysis in Fig. 1(b). There are same

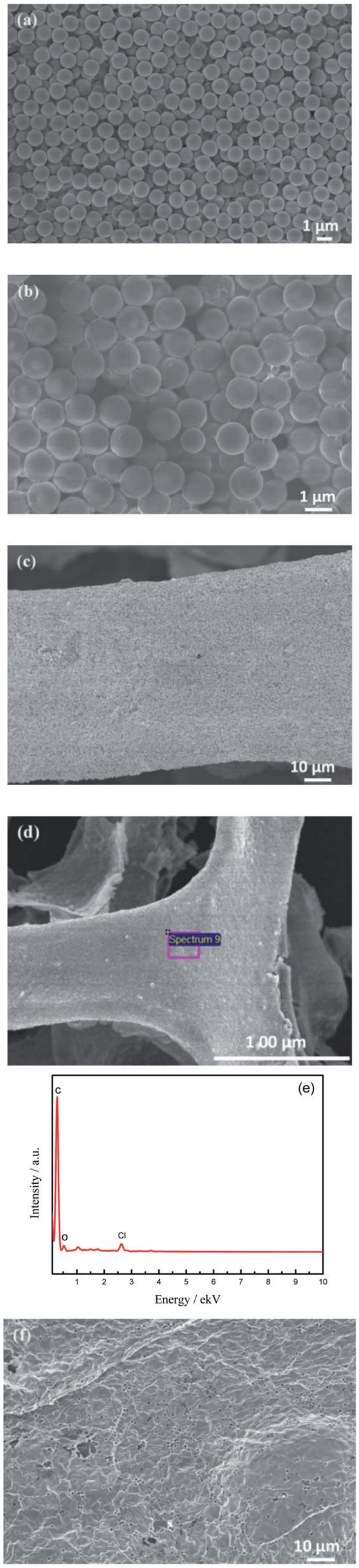

Fig. 1 SEM images of PS microspheres (a), GO/PS (b), GO/PS@Ni (c), GO/PS removal Ni (d), EDS spectrum of GO/PS removal Ni (e), and 3D-Gr (f).

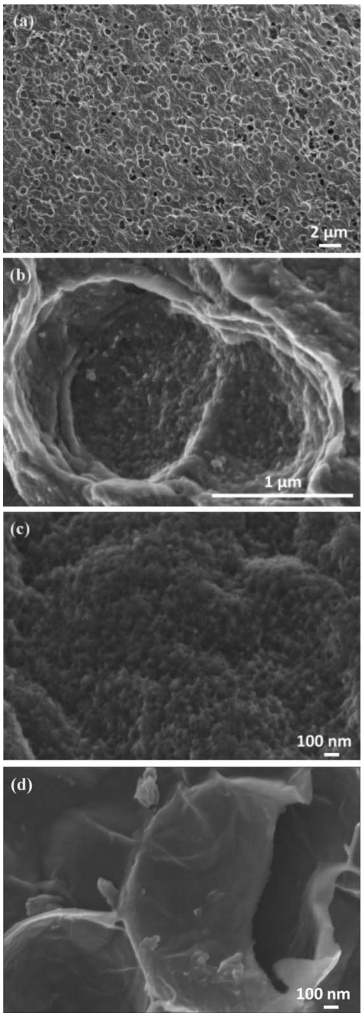

Fig. 2 SEM images of 3D-hpGr after (a–c) and before (d) KOH activation.

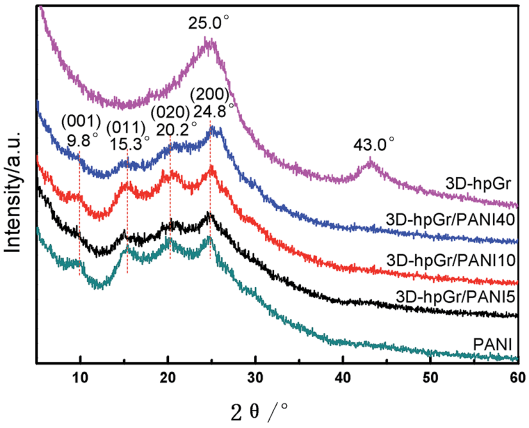

Fig. 3 XRD patterns of 3D-hpGr, pure PANI, 3D-hpGr/PANI5, 3D-hpGr/PANI10, and 3D-hpGr/PANI40.

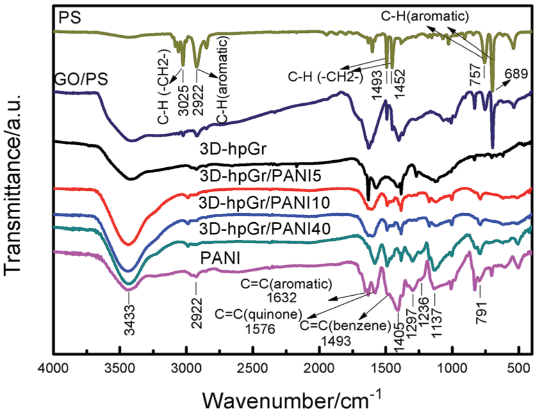

Fig. 4 FT-IR spectra of PS, GO/PS, 3D-hpGr, pure PANI, 3D-hpGr/PANI5, 3D-hpGr/PANI10, and 3D-hpGr/PANI40.

absorption bands around 3433, 2922, and 791 cm^{-1} for all samples except PS, corresponding to the stretching vibration of O–H, the stretching vibration of the aromatic C–H/N–H, and the in-plane bending absorption vibration of benzene rings, respectively. The absorption band around 1632, 1576, 1380, and 1127 cm^{-1} of 3D-hpGr is due to the bending vibration of aromatic C═C, the stretching vibration of aromatic C═C, vibrations of carboxy C–O in C–OH/C–O–C, and in-plane bending of O–H.[22] Absorption peaks at 1576 and 1493 cm^{-1} are attributed to the stretching vibration of C═C in quinone rings and benzene rings, respectively. 1137 cm^{-1} belongs to the characteristic absorption peak of C═N in quinone rings, indicating that the PANI is doped. 1297 cm^{-1} is attributed to the stretching vibration of C–N in quinone rings, 1236 cm^{-1} is attributed to the stretching vibration of C–N in benzene rings. These absorption peaks indicate PNAI is in the intermediate oxidation state. There are several same absorption peaks in spectra of 3D-hpGr/PANI5, 3D-hpGr/PANI10, and 3D-hpGr/PANI40, but there are some different for the peak's shape and the absorption intensity, absorption peaks around 1493, 1297 and 1137 cm^{-1} increase with the increase of 3D-hpGr, indicating that characteristics of quinone rings and benzene rings structure are markedly enhanced.

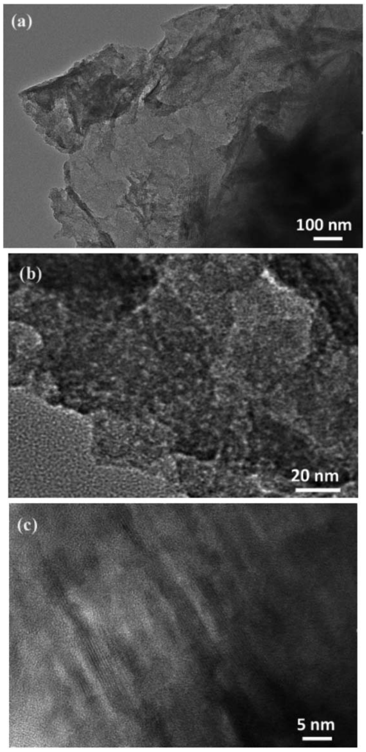

Fig. 5 TEM (a) and HRTEM (b and c) images of 3D-hpGr.

Fig. 5(a) is a TEM image of 3D-hpGr, and Fig. 5(b) and (c) are HRTEM images of 3D-hpGr. It can be clearly seen from Fig. 5(a) that the graphene sheet is very thin, but the specific number of layers cannot be inferred from the TEM. The obvious mesoporous structure can be seen from Fig. 5(a) and (b). Some of the lattice stripes of graphene can be observed from the HRTEM image in Fig. 5(c), the incomplete lattice stripes may be due to a large number of defects formed during the KOH activation

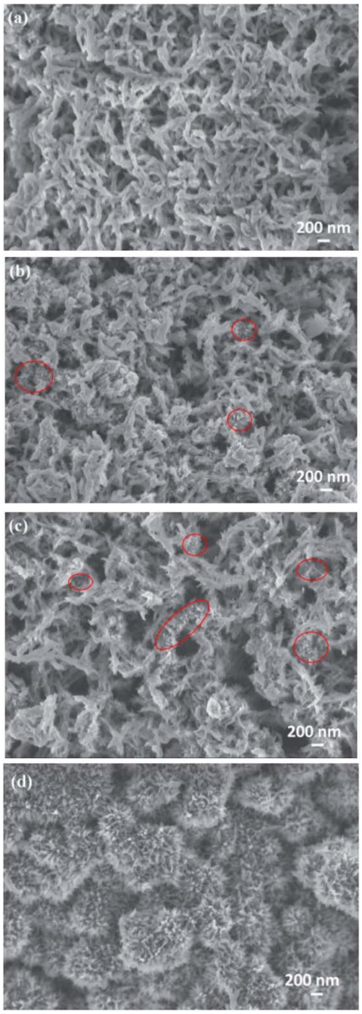

Fig. 6 SEM images of pure PANI (a), 3D hp-rGO/PANI5 (b), 3D hp-rGO/PANI10 (c), and 3D hp-rGO/PAN40 (d).

process, and it may be owing to the incomplete reduction of GO as well.

SEM images of pure PANI, 3D-hpGr/PANI5, 3D-hpGr/PANI10, and 3D-hpGr/PANI40 are shown in Fig. 6. Pure PANI (Fig. 6(a)) appears cross-linking nanorods with the diameter of about 80 nm. After doping with 5% (Fig. 6(b)) and 10% (Fig. 6(c)) of 3D-hpGr, it can be seen that much thinner and shorter PANI nanowires formed, marked by red circles. As the 3D-hpGr increased to 40%, no nanorods can be observed, uniform nanowire arrays grow on the surface of 3D-hpGr sheets, the larger specific surface area is favorable for the interaction of the active materials with the electrolyte.

Fig. 7 shows the CV curves of pure PANI, 3D-hpGr/PANI5, 3D-hpGr/PANI10, and 3D-hpGr/PANI40 at the scan rate of 5, 10, 25, 50 and 100 mV s^{-1} in a 1 M H_2SO_4 electrolyte, respectively. The CV curves of pure PANI display charge and discharge reversibility, but the potential drops at the initial of discharge are obvious due to the internal resistance. The CV curves of 3D-hpGr/PANI composites exhibit good charge and discharge reversibility, and significant redox peaks indicate the typical pseudocapacitance characterization. By comparison, the integrated area of the CV curve gradually increases with the increase of 3D-hpGr, indicating that the introduction of 3D-hpGr is favorable for improving the rate capability.

Fig. 7 shows the CV curves of pure PANI, 3D-hpGr/PANI5, 3D-hpGr/PANI10, and 3D-hpGr/PANI40 at the scan rate of 5, 10, 25, 50 and 100 mV s^{-1} in a 1 M H_2SO_4 electrolyte, respectively. Pure PANI displays charge and discharge reversibility, but the potential drops are on the high side, indicating the internal resistance is large. 3D-hpGr/PANI composites exhibit good charge and discharge reversibility, and significant redox peaks indicate the typical pseudocapacitance characterization. By comparison, the CV curves gradually tend to horizontal with the increase of 3D-hpGr, indicating that the introduction of 3D-hpGr is favorable for improving the rate capability.

Fig. 8 depicts the Nyquist plots of pure PANI, 3D-hpGr/PANI5, 3D-hpGr/PANI10, and 3D-hpGr/PANI40. The obvious semicircles at the high frequency region can be seen. The straight lines at the low frequency region are almost parallel to the vertical axis, which reflects the good capacity owing to the fast and reversible redox. The equivalent series resistance (R_s) and charge transfer resistance (R_{ct}) of pure PANI, 3D-hpGr/PANI5, 3D-hpGr/PANI10, and 3D-hpGr/PANI40 are shown in Table 1. It can be seen that the 3D-hpGr/PANI40 has the lowest R_{ct} (0.382 Ω) and R_s (0.077 Ω). The low R_s and R_{ct} mean excellent electrical conductivity and fast charge transfer at the interface between the electrode and electrolyte.

Fig. 9 shows CD curves of pure PANI, 3D-hpGr/PANI5, 3D-hpGr/PANI10 and 3D-hpGr/PANI40. The C_s and potential drop of pure PANI, 3D-hpGr/PANI5, 3D-hpGr/PANI10, and 3D-hpGr/PANI40 are shown in Table 1 as well. The potential drop decreases with the increase of 3D-hpGr, and the potential drop of 3D-hpGr/PANI40 is the lowest. The C_s of 3D-hpGr/PANI decreases first and then increases with the addition of 3D-hpGr. The C_s of 3D-hpGr/PANI5 and 3D-hpGr/PANI10 are lower than pure PANI, which may be owing to the low mass ratio of 3D-hpGr fails to control the morphology of PANI effectively, while the low electric double-layer C_s of 3D-hpGr leads to the decrease of the composites' C_s. The C_s of 3D-hpGr/PANI40 is 573 F g^{-1} at 0.5 A g^{-1}, which is 36.8% higher than that of pure PANI (419 F g^{-1}), indicating that the proper introduction of 3D-hpGr benefits for improving the electrochemical performance of composites.

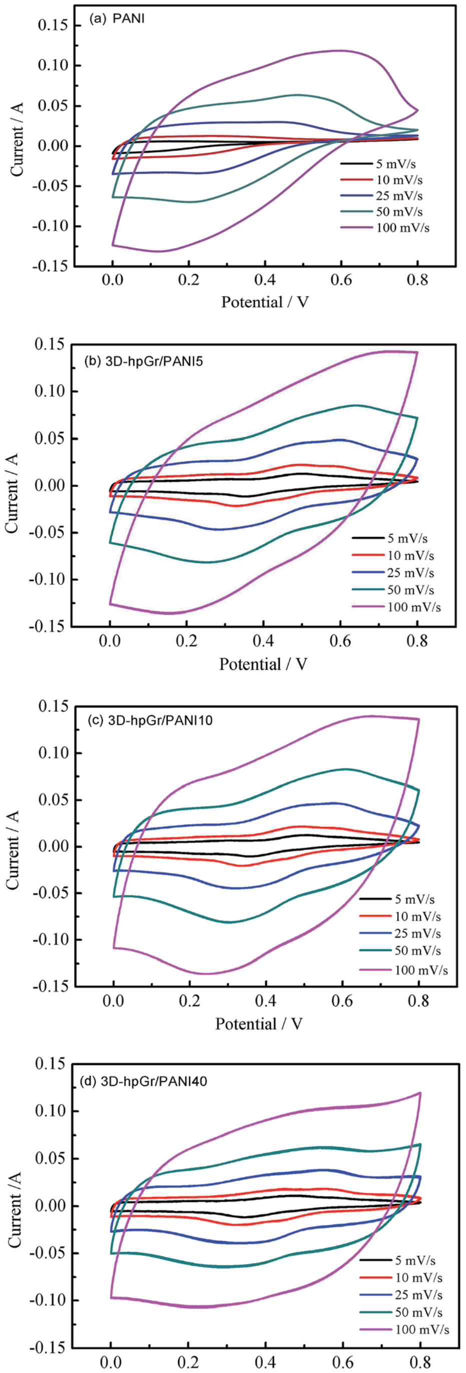

Fig. 7 CV curves of pure PANI, 3D-hpGr/PANI5, 3D-hpGr/PANI10, and 3D-hpGr/PANI40.

Fig. 10 is the cycling stability of pure PANI, 3D-hpGr/PANI5, 3D-hpGr/PANI10, and 3D-hpGr/PANI40 at 1.0 A g^{-1} for 1000 cycles of charge and discharge, and their retention ratio at

Table 1 R_s, R_{ct}, C_s, the retention ratio, power density and energy density of pure PANI, 3D-hpGr/PANI5, 3D-hpGr/PANI10, and 3D-hpGr/PANI40

Samples	R_s	R_{ct}	C_s @ 0.5 A g^{-1} (F g^{-1})	Potential drop (V)	Retention ratio @ 1 A g^{-1} (1000 cycles)	Power density (kW kg^{-1})	Energy density (W h kg^{-1})
PANI	0.122	0.466	419	0.339	69%	0.445	11.1
3D-hpGr/PANI5	0.096	0.441	366	0.254	76%	0.463	13.8
3D-hpGr/PANI10	0.100	0.440	360	0.192	78%	0.572	16.7
3D-hpGr/PANI40	0.077	0.382	573	0.139	84%	0.709	31.2

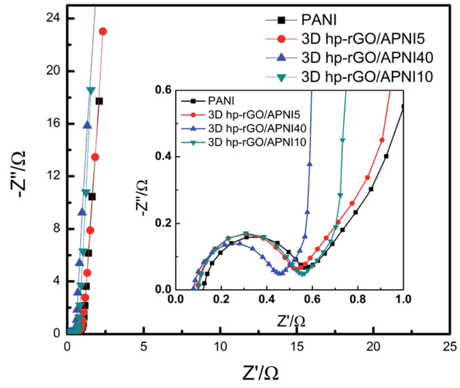

Fig. 8 Nyquist plots of pure PANI, 3D-hpGr/PANI5, 3D-hpGr/PANI10, and 3D-hpGr/PANI40.

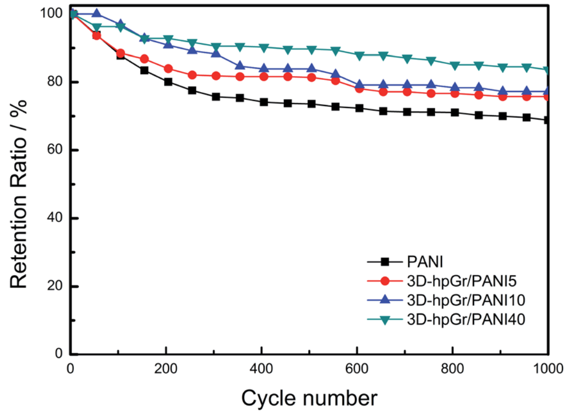

Fig. 10 Cycling stability of pure PANI, 3D-hpGr/PANI5, 3D-hpGr/PANI10, and 3D-hpGr/PANI40 at 1.0 A g^{-1}.

1.0 A g^{-1} after 1000 cycles are also shown in Table 1. The C_s of 3D-hpGr/PANI40 still reaches 84% of its original one at 1.0 A g^{-1} after 1000 cycles of charge and discharge, while the retention ratios of 3D-hpGr/PANI10 and 3D-hpGr/PANI5 are 78% and 76%, respectively. The cycling stability of the 3D-hpGr/PANI composites are all higher than that of pure PANI (69%), so it is concluded that the cycling stability of 3D-hpGr/PANI has been enhanced after combining with 3D-hpGr.

The power density and energy density of pure PANI, 3D-hpGr/PANI5, 3D-hpGr/PANI10, and 3D-hpGr/PANI40 are shown in Table 1 as well. Although the C_s of 3D-hpGr/PANI5 and 3D-hpGr/PANI10 are lower than pure PANI, the energy densities of composites are all improved because the potential drops decrease after the introduction of 3D-hpGr. Especially worth mentioning is that the energy density of 3D-hpGr/PANI40 reaches 31.2 W h kg^{-1} at a power density of 0.709 kW kg^{-1}, while the energy density of pure PANI is 11.1 W h kg^{-1} at a power density of 0.445 kW kg^{-1}.

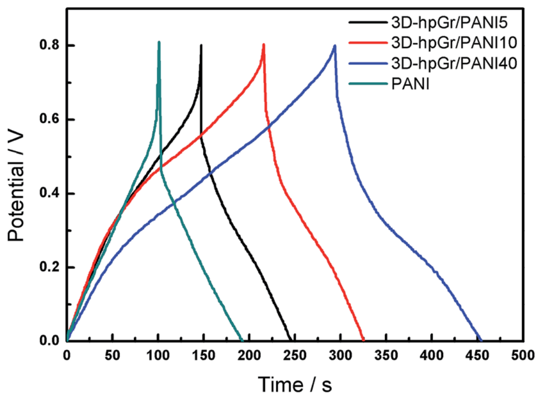

Fig. 9 CD curves of pure PANI, 3D-hpGr/PANI5, 3D-hpGr/PANI10, and 3D-hpGr/PANI40 at 0.5 A g^{-1}.

4 Conclusions

Combining template and KOH activation methods can effectively construct 3D hierarchical porous structure graphene/PANI composites. Different morphology can be obtained by controlling the composition. 3D-hpGr/PANI40 possesses uniform PANI nanowire arrays on the 3D hierarchical porous graphene. The ion-diffusion and charge-transfer resistances of the hierarchical porous composites are decreased. The potential drop decreases with the increase of 3D-hpGr. 3D hierarchical porous graphene can effectively improve the electrochemical performance of PANI, especially for the specific capacitance, cycling stability and energy density. The enhanced electrochemical performance may be due to two aspects: (1) the 3D hierarchical porous structure of 3D-hpGr is favorable for electrolyte transport through porous channels and fast charge transfer at the interface between the electrode and electrolyte; (2) the electrode's volume and structure changes during the charge–discharge cycling are controlled to the lower degree by 3D porous structure graphene. 3D hierarchical porous graphene/polyaniline composites maybe become promising electrode materials for future application in supercapacitors.

Author contributions

Conceptualization, Zhaoxia Hou; methodology, Lingxi Kong, Lanwei Zhao and Lirong Yang; data curation, Shengnan Zou; writing—review and editing, Zhaoxia Hou.

Funding

This research was funded by the Program of the National Natural Science Foundation of China (No. 51472166) and Liaoning BaiQianWan Talents Program.

Conflicts of interest

The authors declare no conflict of interest. The funders had no role in the design of the study; in the collection, analyses, or interpretation of data; in the writing of the manuscript, or in the decision to publish the results.

References

1 K. Wang, X. Zhang, C. Li, X. Sun, Q. Meng, Y. Ma and Z. Wei, Chemically crosslinked hydrogel film leads to integrated flexible supercapacitors with superior performance, *Adv. Mater.*, 2015, **27**, 7451–7457, DOI: 10.1002/adma.201503543.

2 L. J. Deng, Y. Z. Gu, Y. H. Gao, Z. Y. Ma and G. Fan, Carbon nanotubes/holey graphene hybrid film as binder-free electrode for flexible supercapacitors, *J. Colloid Interface Sci.*, 2017, **494**, 355–362, DOI: 10.1016/j.jcis.2017.01.062.

3 J. Y. Luo, J. Kim and J. X. Huang, Material processing of chemically modified graphene: some challenges and solutions, *Acc. Chem. Res.*, 2013, **46**, 2225–2234, DOI: 10.1021/ar300180n.

4 J. Ji, Y. Li, W. Peng, G. Zhang, F. Zhang and X. Fan, Advanced graphene-based binder-free electrodes for high-performance energy storage, *Adv. Mater.*, 2015, **27**, 5264–5279, DOI: 10.1002/adma.201501115.

5 T. S. Yang, H. Lin, X. R. Zheng, K. P. Loh and B. H. Jia, Tailoring pores in graphene-based materials: from generation to applications, *J. Mater. Chem. A*, 2017, **5**, 16537–16558, DOI: 10.1039/C7TA04692H.

6 X. Xu, Y. Liu, M. Wang, X. X. Yang, C. Zhu, T. Lu, R. Zhao and L. K. Pan, Design and fabrication of mesoporous graphene *via* carbothermal reaction for highly efficient capacitive deionization, *Electrochim. Acta*, 2016, **188**, 406–413, DOI: 10.1016/j.electacta.2015.12.028.

7 S. G. Dai, Z. Liu, B. Zhao, J. H. Zeng, H. Hu, Q. B. Zheng, D. C. Chen, C. Qu, D. Dang and M. L. Lin, A high-performance supercapacitor electrode based on N-doped porous graphene, *J. Power Sources*, 2018, **387**, 43–48, DOI: 10.1016/j.jpowsour.2018.03.055.

8 H. H. Liu, H. L. Zhang, H. B. Xu, T. P. Luo, Z. T. Sui and Y. Zhang, In situ self-sacrificed template synthesis of vanadium nitride/nitrogen-doped graphene nanocomposites for electrochemical capacitors, *Nanoscale*, 2018, **10**, 5246–5253, DOI: 10.1039/C7NR08985F.

9 Y. Lin, Y. Liao, Z. Chen and J. W. Connell, Holey graphene: a unique structural derivative of graphene, *Mater. Res. Lett.*, 2017, **5**, 209–234, DOI: 10.1080/21663831.2016.1271047.

10 R. R. Nair, H. A. Wu, P. N. Jayaram, I. V. Grigorieva and A. K. Geim, Unimpeded permeation of water through helium-leak-tight graphene-based membranes, *Science*, 2012, **335**, 442–444, DOI: 10.1126/science.1211694.

11 V. Strauss, K. Marsh, M. D. Kowal, M. El-Kady and R. B. Kaner, A simple route to porous graphene from carbon nanodots for supercapacitor applications, *Adv. Mater.*, 2018, **30**, 1704449–1704458, DOI: 10.1002/adma.201704449.

12 Y. H. Xie, X. X. Sheng, D. L. Xie, Z. X. Liu, X. Y. Zhang and L. Zhong, Fabricating graphene hydrogels with controllable pore structure *via* one-step chemical reduction process, *Carbon*, 2016, **109**, 673–680, DOI: 10.1016/j.carbon.2016.08.079.

13 B. Song, F. Wu, Y. T. Zhu, Z. X. Hou, K. Moon and C. P. Wong, Effect of polymer binders on graphene-based free-standing electrodes for supercapacitors, *Electrochim. Acta*, 2018, **267**, 213–221, DOI: 10.1016/j.electacta.2018.02.072.

14 L. L. Zhang, D. Huang, N. T. Hu, C. Yang, M. Li, H. Wei, Z. Yang, Y. J. Su and Y. F. Zhang, Three-dimensional structures of graphene/polyaniline hybrid films constructed by steamed water for high-performance supercapacitors, *J. Power Sources*, 2017, **342**, 1–8, DOI: 10.1016/j.jpowsour.2016.11.068.

15 X. D. Hong, B. B. Zhang, E. Murphy, J. L. Zou and F. Kim, Three-dimensional reduced graphene oxide/polyaniline nanocomposite film prepared by diffusion driven layer-by-layer assembly for high-performance supercapacitors, *J. Power Sources*, 2017, **343**, 60–66, DOI: 10.1016/j.jpowsour.2017.01.034.

16 Y. Liu, Y. Ma, S. Y. Guang, F. Y. Ke and H. Y. Xu, Polyaniline-graphene composites with a three-dimentional array-based nanostructure for high performance supercapacitors, *Carbon*, 2015, **83**, 79–89, DOI: 10.1016/j.carbon.2014.11.026.

17 K. Wang, L. W. Li, W. Xue, S. Z. Zhou, Y. Lan, H. W. Zhang and Z. Q. Sui, Electrodeposition synthesis of PANI/MnO_2/graphene composite materials and its electrochemical performance, *Int. J. Electrochem. Sci.*, 2017, **12**, 8306–8314, DOI: 10.20964/2017.09.06.

18 J. W. Luo, W. B. Zhong, Y. B. Zou, C. L. Xiong and W. T. Yang, Preparation of morphology-controllable polyaniline and polyaniline/graphene hydrogels for high performance binder-free supercapacitor electrodes, *J. Power Sources*, 2016, **319**, 73–81, DOI: 10.1016/j.jpowsour.2016.04.004.

19 X. Lu, L. Li, B. Song, K. Moon, N. N. Hu, G. L. Liao, T. L. Shi and C. P. Wong, Mechanistic investigation of the graphene functionalization using p-phenylenediamine and its application for supercapacitors, *Nano Energy*, 2015, **17**, 160–170, DOI: 10.1016/j.nanoen.2015.08.011.

20 T. A. Saleh, Nanocomposite of carbon nanotubes/silica nanoparticles and their use for adsorption of Pb(II): from surface properties to sorption mechanism, *Desalin. Water Treat.*, 2016, **23**, 10730–10744, DOI: 10.1080/19443994.2015.1036784.

21 T. A. Saleh, Simultaneous adsorptive desulfurization of diesel fuel over bimetallic nanoparticles loaded on activated carbon, *J. Clean. Prod.*, 2017, **172**, 2123–2132, DOI: 10.1016/j.jclepro.2017.11.208.

22 T. A. Saleh, Mercury sorption by silica/carbon nanotubes and silica/activated carbon: a comparison study, *J. Water Supply: Res. Technol.–AQUA*, 2015, **64**(8), 892–903, DOI: 10.2166/aqua.2015.050.